

# Source mechanisms of dike-induced earthquakes in the Dabbahu-Manda Hararo rift segment in Afar, Ethiopia: implications for faulting above dikes

Manahloh Belachew,<sup>1,2</sup> C. Ebinger<sup>1</sup> and D. Côté<sup>1</sup>

<sup>1</sup>Department of Earth and Environmental Sciences, University of Rochester, Rochester, NY 14627, USA. E-mail: manahloh@yahoo.com

<sup>2</sup>Institute of Geophysics, Space Science and Astronomy, Addis Ababa University, PO Box 1176, Addis Ababa, Ethiopia

Accepted 2012 November 19. Received 2012 November 16; in original form 2011 October 11

## SUMMARY

The process of dike emplacement changes the stress field in the intruded region, causing swarms of migrating earthquakes. We determine source mechanisms of the largest earthquakes ( $M_L \geq 3.5$ ) induced by the emplacement of two large volume dikes along an incipient seafloor spreading segment in Afar, Ethiopia to determine their space-time relations. Given the possibility of complex source mechanisms during dike emplacement, we solved for four different source models: double couple (DC), DC + isotropic (DC + ISO), deviatoric (DVMT), and full moment tensor (FMT). The solutions obtained using the different models indicate that the earthquakes have non-double couple components. The best double-couple mechanisms, which are mainly normal faulting with small strike-slip components, have slip planes nearly perpendicular to the geodetically determined plate opening direction. Most of these earthquakes are low-frequency earthquakes with peak frequencies  $\leq 2$  Hz, and they occurred during the propagation phase of the dikes. The space-time distribution of the source mechanisms with respect to the migrating patterns of seismicity during dike emplacement, the shallow source depths estimated, the lack of mechanisms with  $\sim 90^\circ$  rotated P-axes from the regional maximum compressive stress and the non-double couple nature of the mechanisms indicate that the largest magnitude earthquakes are generated mainly by normal faulting above the dikes probably with some component of tensile opening under the influence of dike-related fluids. These observations suggest that normal faulting above dikes is the main process of seismic energy release during dike intrusions. Assuming that faults above dikes follow length-displacement relations found for tectonic earthquakes, total seismic slips of 0.8 m and 1.3 m are estimated for the November 2007 and October 2008 dikes, respectively. Similarity of the total slip estimates from the largest earthquakes and from elastic dislocation model estimates of normal fault slips and the larger total seismic versus geodetic moment deficits indicates that most of the plate opening by dike intrusion is accommodated aseismically. Our results show that during dike intrusions surface faulting above dikes is the main process that controls the development of rift zone geomorphology and topography.

**Key words:** Earthquake source observations; Volcano seismology; Continental tectonics; extensional; Africa.

## 1 INTRODUCTION

Earthquakes induced by a laterally propagating dike occur ahead of the dike tip, above it and in the regions adjacent to the dike walls (e.g. Rubin & Pollard 1988; Rubin 1992; Toda *et al.* 2002). However, their spatio-temporal distribution and faulting types are not well constrained. Crack/elastic models reveal that dike intrusions increase the horizontal compressive stress in the host rock on both sides of the dike plane, locking faults beside the dike from slipping (e.g. Pollard *et al.* 1983; Rubin 1992; Rubin & Pollard 1988). On the other hand, models of near-field stress rate changes predict small

magnitude earthquakes in the walls of an inflating dike (Bonafede & Danesi 1997; Toda *et al.* 2002; Roman *et al.* 2004; Roman 2005). Stress concentrations mainly caused by increased pore pressure at the tips of propagating blade-shaped dikes result in seismicity (Rubin & Pollard 1988; Rubin 1992; Wills & Buck 1997; Rubin & Gillard 1998; Rubin *et al.* 1998).

Between 2005 and 2010 fourteen large volume dikes intruded the Dabbahu-Manda Hararo (DMH) rift segment (Grandin *et al.* 2009; Ebinger *et al.* 2010). Among these dikes, 9 are well recorded by temporary seismic networks. Source mechanisms were determined for the largest earthquakes ( $5 \leq M_w \leq 5.4$ ) from the first dike of the

sequence by waveform modeling of regional seismic data (Ayele *et al.* 2009), and using polarity readings for the largest post-diking earthquakes using a 9-station network (Ebinger *et al.* 2008). Both of these studies assumed double couple mechanisms, and showed dominantly normal faulting mechanisms consistent with surface faulting observations (Rowland *et al.* 2007).

The main aim of this study is to identify where and when during a dike intrusion specific types of faulting mechanism occur. In order to achieve this aim we investigate various source models to (1) to improve source depth estimates moderately constrained by the array geometry; and (2) to correlate the seismic moment release with specific aspects of the dike injection process, enabling comparison with independent geodetic and field constraints on fault slip and length (e.g. Rowland *et al.* 2007). Improved depth estimates enable us to determine where the studied dike-induced earthquakes and their associated faulting mechanisms occur during dike propagation. Here source mechanisms of the largest earthquakes induced by two of the dike intrusions in the DMH rift segment are analyzed.

Earthquakes related to the other dikes and fissural eruptions were too small in magnitude to obtain reasonable results with the methods in this study.

The computed source mechanisms, their space-time distribution with respect to the epicentral migration, and their shallow depths indicate that shear failure causing faulting above the dikes is the dominant process generating the largest earthquakes during dike intrusions. Thus, seismic energy release during dike intrusions is primarily due to faulting above the dikes, with the process of dike emplacement occurring largely aseismically.

## 2 TECTONIC SETTING

The ~300 km-wide Afar Depression marks the zone of linkage between the northern Main Ethiopian Rift, the southern Red Sea, and the western Gulf of Aden, forming a rift–rift–rift triple junction between the Nubian, Somalian and Arabian Plates (McKenzie *et al.* 1970) (Fig. 1). Since ~3 Ma the ~60 km-long Quaternary

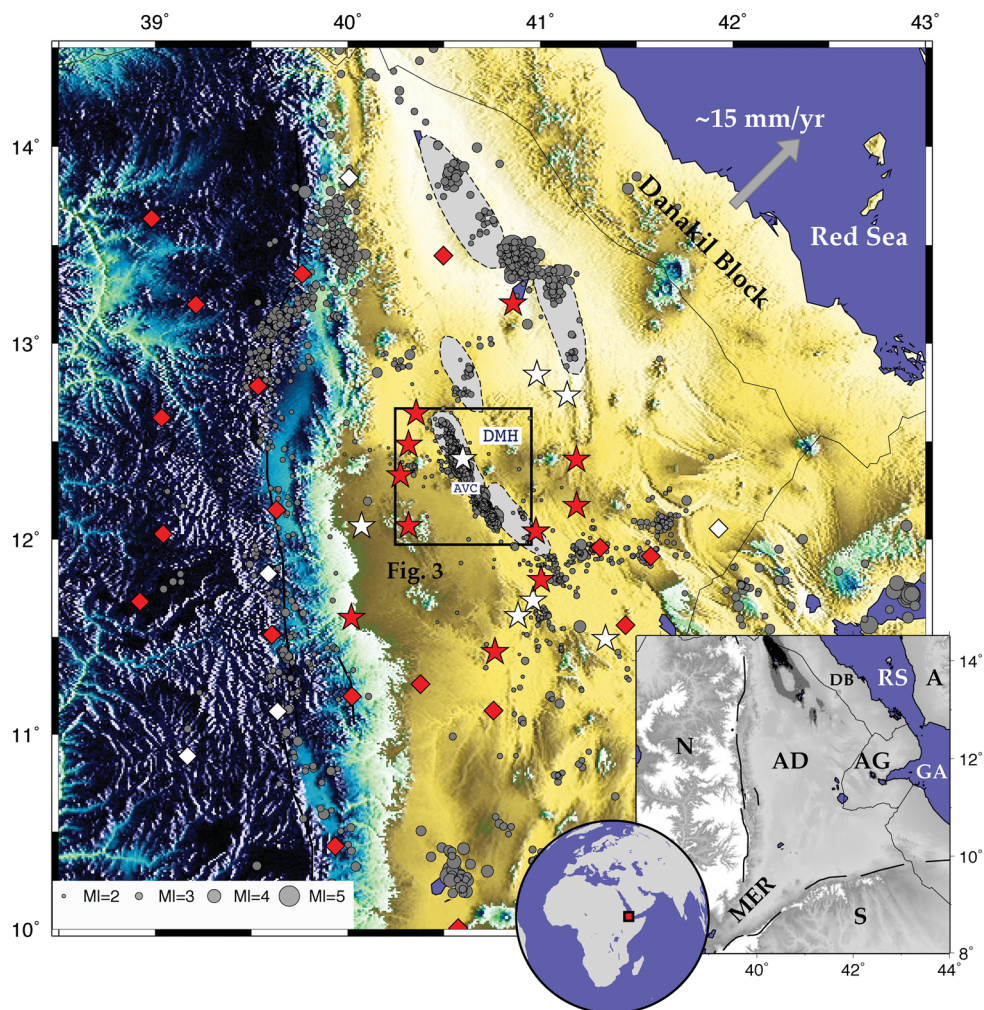


**Figure 1.** Seismicity of the Afar depression recorded between March 2007 and October 2009 on the combined IRIS-PASSCAL (stars) and SEIS-UK (diamonds) seismic network. Stations used for the source mechanism study are shown as red stars and diamonds. Gray circles represent earthquakes scaled by magnitude (Belachew *et al.* 2011). Heavy black lines show Oligocene-Recent border faults of the southern Red Sea. Grey filled regions with dashed-line edges indicate the Quaternary magmatic segments that are the locus of faulting and magmatism. The DMH rift segment is shown. The AVC where the main feeder zone is located is also shown. Motion of the Arabian plate relative to stable Nubian plate is shown as a grey arrow (Vigny *et al.* 2006). The rectangle encompasses the DMH rift segment that has been intruded by large volume dikes since September 2005, and the location of Fig. 3. Inset shows the regional tectonic blocks and rifts. Acronyms are: AG, Asal-Ghoubbet magmatic segments; A, Arabian Plate; DB, Danakil micro-plate; S, Somalian plate; GA, Gulf of Aden; MER, Main Ethiopian Rift; N, Nubian Plate; RS, Red Sea.

magmatic segments within the Afar depression are the loci of active deformation, and are characterized by aligned cones, small offset faults and fissures (e.g. Hayward & Ebinger 1996; Manighetti *et al.* 2001). The DMH rift is part of the southern subaerial extension of the Red Sea rift (e.g. Barberi & Varet 1977; Manighetti *et al.* 2001) (Fig. 1).

Between 2005 and 2010, 14 large volume dikes intruded this rift segment (e.g. Hamling *et al.* 2009; Ebinger *et al.* 2010; Belachew *et al.* 2011). The rifting cycle started by intrusion of a mega-dike in 2005 along the ~70 km-long of the DMH segment, resulting in rift-perpendicular opening of up to 8 m (Wright *et al.* 2006; Grandin *et al.* 2009) and surface slips of up to 5 m on some faults (Rowland *et al.* 2007). Geodetic and seismic evidence show this dike was fed both from beneath the Dabbahu volcano to the north and from beneath the mid-segment Ado'Ale Volcanic Complex (AVC) (Wright *et al.* 2006; Ebinger *et al.* 2008; Ayele *et al.* 2009; Grandin *et al.* 2009) (Fig. 1).

Since the first mega-dike 13 relatively small volume intrusions were fed from a mid-segment magma chamber located beneath the centre of the AVC (Keir *et al.* 2009; Grandin *et al.* 2010; Hamling *et al.* 2010; Belachew *et al.* 2011; Grandin *et al.* 2011). This feeder zone is marked by a seismicity gap consistent with the presence of a hot, fluid-rich, and weak region that extends to the near surface (Belachew *et al.* 2011). Since the onset of the current rifting cycle, a sequence of dikes propagated to the north along the rift followed by another sequence propagating to the south, with only three of the dikes producing fissural eruptions (e.g. Hamling *et al.* 2009; Belachew *et al.* 2011; Grandin *et al.* 2011). Seismicity patterns of 7 of the well monitored dikes indicate that the dikes propagated faster to the north than to the south, suggesting the high level of faulting and fracturing and release of tectonic stress during the 2005 mega-dike facilitated dike propagation (Belachew *et al.* 2011). More than 80 per cent of the seismic energy during intrusions is released during the propagation phase, and the earthquakes mainly represent faulting above and ahead of the propagating dikes (Belachew *et al.* 2011).

The total seismic moment release for the combined processes at the dike tip, within the dike walls and faulting above the dike of the November 2007 and October 2008 dikes is 3.3 and 2.3 per cent, respectively, of the geodetic moment estimated from elastic dislocation models (Hamling *et al.* 2009; Belachew *et al.* 2011). This indicates that most of the plate boundary deformation occurs aseismically. Yet, it remains unclear how the seismic strain is partitioned between faulting above the dike, at the propagating dike tip or in the wall rock to the dike. Hamling *et al.* (2009) estimated slips on normal faults for individual dikes based on elastic dislocation modeling of InSAR data and obtained values of 1.9 m and 1.3 m for the November and October dikes, respectively. The geodetic moment estimates obtained from the surface fault slip estimates are 10 and 13 per cent of the total geodetic moment estimates for November 2007 and October 2008 dike intrusions, respectively.

### 3 DATA AND METHODS

#### 3.1 Data

As part of the collaborative Afar Consortium project, which involves US, UK and Ethiopian universities, 44 IRIS-PASSCAL and SEIS-UK 3-component broadband seismometers were deployed and operated between March 2007 and October 2009 across a ~350 km × 350 km region within the Afar Depression and on the western

plateau (Fig. 1). Within the Afar Depression, due to the remoteness of the region, temporary seismic stations could only be deployed in villages and guarded government facilities, dictating the geometry of the network. Most of the stations operated continuously with sampling rate of 50 Hz. A total of ~5320 earthquakes were recorded on 4 or more stations from within the Afar Depression and adjacent regions during the two and a half year operation period of the network. Almost half of the earthquakes occurred during the dike intrusion episodes along the DMH rift segment (Fig. 1). Hypocenter accuracy for the earthquakes of about ±1 km in horizontal directions and ±3 km in depth is obtained (Belachew *et al.* 2011). For this study earthquakes from the DMH rift segment with  $M_L \geq 3.5$ , with good quality waveforms and recorded on stations at regional distances between 50 and 230 km are used for the inversions.

#### 3.2 Moment tensor inversion and grid search approaches

Using three-component broadband digital waveforms at regional distances we solved for double couple (DC), deviatoric (DVMT), DC plus isotropic (DC + ISO) and full moment tensor (FMT) source models. A moment tensor can be decomposed into three components, including a double-couple component, an isotropic component, and a compensated linear vector dipole (CLVD) component (e.g. Knopoff & Randall 1970; Jost & Herrmann 1989). The isotropic component defines a volume change (either implosion or explosion) at the seismic source, and the CLVD component describes the compensation for non-double couple effects on a principal axis. The DC and CLVD components are also called deviatoric components, defining a geometry change at the seismic source. The pure DC model assumes that the earthquake source is best modeled by shear faulting on planar faults, and *a priori* sets the CLVD and the isotropic components to zero. The DC + ISO model is used for sources that are a combination of simultaneous shear slip and volumetric change with zero CLVD component (e.g. Dreger & Woods 2002; Templeton & Dreger 2006). The DVMT solution, which sets the volumetric components to zero and solves only for the DC and CLVD components, is used to describe volume-conserving source processes that deviate from pure DC mechanisms. Such source processes are observed in cases where fluid flows rapidly into a crack causing no volume change (e.g. Julian & Sipkin 1985). The FMT model solves for all the three source components of the moment tensor, and is used to describe processes involving both shear and tensile opening.

The corrected form of the linear time domain moment tensor inversion algorithm, which uses long-period full waveforms recorded at regional distances, is used to determine the DVMT and FMT solutions (Dreger *et al.* 2000; Minson & Dreger 2008). For the DC and DC + ISO models, a grid search approach iterating over strike, dip, rake, DC moment and isotropic moment over the entire model space is used (Dreger *et al.* 2000; Dreger & Woods 2002; Templeton & Dreger 2006). A coarse grid search is first performed to determine rough estimates of the mechanisms. This is followed by a fine grid search for the best solutions around the rough estimates in 5-degree increments.

These methods (except the DC method) have been tested in several source studies in volcanic earthquakes, nuclear explosions, and using synthetic data (Dreger *et al.* 2000; Dreger & Woods 2002; Templeton & Dreger 2006; Minson *et al.* 2007; Minson & Dreger 2008). The studies showed that the methods are capable of recovering the non-double components of source mechanisms. The methods use full waveforms from the vertical, radial and transverse

**Table 1.** One-dimensional velocity model used to calculate Green's functions (after Jacques *et al.* 1999, and  $V_p/V_s = 1.8$  from Belachew *et al.* 2011).

Thickness (km)	P-wave velocity (km/s)	S-wave velocity (km/s)	Density (kg/m <sup>3</sup> )	$Q_\alpha$	$Q_\beta$
3.0	4.50	2.50	2200	600	300
5.0	6.20	3.44	2600	600	300
17.0	6.80	3.78	2800	600	300
$\infty$	8.04	4.50	3300	600	300

**Table 2.** List of events for the earthquakes in this study (Hypocenter information are from Belachew *et al.* 2011).

Event	Date (year/month/day)	Time (UT)	Lat. ( $^{\circ}$ N)	Lon. ( $^{\circ}$ E)	Depth (km)	MI
1	2007/11/11	19:47:59	12.203	40.681	3.0	3.5
2	2007/11/11	20:37:33	12.226	40.690	1.4	3.7
3	2007/11/11	21:21:21	12.222	40.691	1.5	4.6
4	2007/11/11	23:53:04	12.206	40.702	3.7	3.8
5	2007/11/12	00:40:17	12.210	40.679	2.4	3.7
6	2007/11/12	02:46:29	12.169	40.721	0.7	3.6
7	2007/11/12	03:24:32	12.168	40.715	1.3	3.6
8	2007/11/12	03:30:11	12.164	40.681	1.0	3.5
9	2007/11/12	23:46:52	12.122	40.744	0.5	3.7
10	2007/11/13	22:26:50	12.123	40.746	0.2	3.5
11	2008/10/17	08:57:35	12.346	40.600	2.9	4.3
12	2008/10/17	09:20:59	12.355	40.589	8.9	4.0
13	2008/10/17	09:24:04	12.360	40.585	3.1	3.7
14	2008/10/17	09:40:38	12.354	40.594	1.3	4.6
15	2008/10/17	10:26:08	12.351	40.586	0.3	3.9
16	2008/10/17	10:57:13	12.361	40.592	1.9	4.7
17	2008/10/17	13:06:07	12.416	40.568	4.2	4.0
18	2008/10/17	14:36:38	12.402	40.566	3.7	3.6
19	2008/10/17	14:47:13	12.403	40.570	3.0	3.6
20	2008/10/17	15:45:20	12.405	40.567	0.9	4.3
21	2008/10/17	20:24:23	12.359	40.592	2.5	4.2
22	2008/10/18	12:56:22	12.363	40.589	8.2	4.1
23	2009/02/11	23:49:18	12.364	40.599	3.9	4.0

components. Green's functions, which form the synthetic seismograms, were computed using the frequency-wave number integration program (FKRPROG) (Saikia 1994) for a one-dimensional velocity model (Table 1). To determine the best source depth synthetic seismograms and deviatoric moment tensors were estimated for depths from 0 km to 10 km in increments of 1 km. The selected depth range is typical of the dike-induced seismicity distribution in the DMH rift segment (Ebinger *et al.* 2008; Belachew *et al.* 2011). The depth that yielded the largest variance reduction (best fit) is chosen as the centroid depth, and we used the selected depth in all of the source modeling. The variance reduction, VR is computed using

$$VR = \left[ 1 - \sum_i \left( \frac{\sqrt{(data_i - synth_i)^2}}{\sqrt{data_i^2}} \right) \right] * 100, \quad (1)$$

where  $data_i$  and  $synth_i$  are the data and synthetics for all stations considered, respectively. The data and synthetic seismograms were bandpass filtered between periods of 20 and 50 s for  $M_w \geq 4$  and between 10 and 50 s for  $M_w \leq 4$ . Stations are considered for the source inversion based on visual inspection of waveform quality, and to ensure good azimuthal coverage with respect to the earthquake.

## 4 RESULTS

Twenty-three solutions with variance reduction values  $>50$  per cent that are obtained using all methods are presented here (Tables 3, 4, S2–S5). These are the largest earthquakes with relatively good quality data. Among the 23 earthquakes studied in this paper only two are reported in the Harvard CMT catalog, where source mechanisms are determined using globally recorded waves and assuming deviatoric source models. The similarity of our DVMT solutions for events 14 and 16 with the Harvard CMT solutions indicates the local velocity model used has little effect on the solutions (Fig. 3). The relative difference in the fit to data between the DC and DC + ISO solutions is smaller than that between the DC and DVMT solutions (Table 3). On average there is an 8 per cent increase in the variance reduction between the DC + ISO and the DVMT solutions. The measures of fit to the data for the DVMT and FMT solutions are almost the same. Fig. 2 shows sample waveform fits and associated DVMT and FMT solution parameters for events 6, 16 and 23, which illustrates the fits obtained for different numbers of stations used. Since the DC, DC + ISO and DVMT models are all represented by five independent moment tensor elements the variation in the misfit values among these models is likely to show the significance of the different components of the source mechanisms. The FMT solutions, which are represented by six independent moment tensor elements, do not provide a significantly improved fit to the data as compared to the DVMT solutions. For some of the events, however, the isotropic components are more than 40 per cent to be considered as artefacts (e.g. events 1 and 23, Table 4). The measure of goodness of fit shows the FMT inversion does not significantly increase from the DVMT solution as expected due to the added source complexity.

The variations in the goodness of fit to the data among the different models could be due to the smaller magnitude of the earthquakes studied and noise (e.g., Nakano *et al.* 2008). Given the relatively

**Table 3.** Comparison of variance reductions (per cent) obtained from the DC, DC + ISO, DVMT and FMT models for the events studied (Table 2).

Event	Depth (km)	DC	DC + ISO	DVMT	FMT
1	1	62.95	62.95	64.2	67.7
2*	2	67.86	67.92	71.6	68.5
3*	2	92.19	92.24	93.0	93.1
4*	6	83.36	85.72	84.4	85.7
5*	2	65.99	66.10	73.3	73.3
6	5	66.42	67.63	67.5	70.3
7	2	59.59	59.59	60.8	61.3
8	2	52.46	52.46	54.2	58.5
9	6	77.43	77.43	87.3	75.0
10*	6	65.10	65.10	64.4	54.5
11*	2	79.60	80.04	86.9	86.9
12	1	73.65	73.97	82.2	82.6
13	2	53.07	53.46	65.8	65.8
14*	1	92.11	92.87	92.3	91.2
15*	1	69.34	69.34	76.8	76.9
16*	1	89.11	89.55	90.5	90.5
17*	2	76.79	76.81	78.9	79.5
18*	2	59.53	59.53	66.1	67.3
19*	2	50.34	50.33	62.5	63.4
20*	2	91.54	93.85	92.7	92.8
21*	1	91.67	91.85	92.8	92.9
22*	1	27.11	27.51	72.5	72.7
23	2	77.48	78.46	79.0	81.0

The best source depths determined from the deviatoric moment tensor inversions are given. \*Low frequency earthquakes.

**Table 4.** Comparison of the percentages of DC, CLVD and ISO components estimated from the deviatoric and FMT inversions. Values to the left are for the deviatoric inversions and to the right are for the FMT inversions. Strike, dip and rake from the deviatoric inversions are also given.

Event	$M_w$	DC (per cent)	CLVD (per cent)	ISO (per cent)	Strike	Dip	Rake
1	3.7	47/17	53/37	0/46	180/360	38/70	-34/-122
2	3.6	35/22	65/50	0/28	98/336	73/30	-115/-35
3	4.6	95/60	5/15	0/25	144/330	67/23	-93/-84
4	3.9	65/54	35/14	0/32	116/353	72/30	-115/-37
5	3.7	68/59	32/32	0/8	126/351	50/50	-123/-57
6	3.6	76/23	24/42	0/35	130/334	56/34	-98/-78
7	3.6	51/30	49/37	0/33	0/124	61/45	-54/-136
8	3.5	49/38	51/40	0/22	116/349	59/44	-124/-47
9	3.5	30/32	70/39	0/28	127/30	77/62	-151/-15
10	3.4	38/47	62/37	0/16	20/128	62/59	-35/146
11	4.4	47/42	53/50	0/9	123/355	61/42	-121/-47
12	4.1	36/24	64/50	0/26	111/348	71/33	-117/-38
13	4.1	68/68	32/31	0/1	352/134	51/45	-64/-119
14	4.9	89/74	11/0	0/26	160/326	71/20	-85/-103
15	3.9	89/60	11/21	0/19	133/349	50/46	-115/-63
16	4.8	87/86	13/10	0/4	159/328	63/28	-85/-100
17	4.1	78/44	22/30	0/25	129/351	69/28	-108/-51
18	3.9	68/30	32/35	0/34	125/352	65/34	-114/-49
19	3.8	30/19	70/50	0/31	111/349	71/34	-118/-36
20	4.5	48/40	52/30	0/30	123/348	68/29	-110/-49
21	4.4	49/30	51/42	0/28	115/346	68/33	-115/-44
22	4.1	96/43	4/23	0/34	152/325	59/32	-86/-96
23	4.1	93/11	7/16	0/73	147/333	49/41	-94/-86

small magnitude of the earthquakes and the minor differences in the variance reduction between the DVMT and FMT solutions, further exploration of the tradeoffs between isotropic and CLVD components is needed to determine whether they can be distinguished. Instead, we use the DVMT with some consideration of the isotropic components, considering the association with a dike episode and the unusually low-frequency content of the majority of earthquakes, and the likelihood that most of events have non-double couple components. This is also done since our main aim is to identify the type of faulting during intrusions (e.g., normal faulting above the dike, strike-slip faulting in wall rocks, etc.), rather than determination of the significance of the different source components.

The best double couple mechanisms are normal faults with a small strike-slip component with the exception of two dominantly strike-slip mechanisms (Fig. 3). The majority of the nodal planes have NNW-SSE strikes and dip 50–80°. These nodal plane orientations are consistent with the strikes of surface fault ruptures measured in the field and from satellite imagery (e.g. Rowland *et al.* 2007; Grandin *et al.* 2009). To account for the sensitivity of the solutions with depth, variance reductions for depths 1–10 km at 1 km increments are considered. The results show that the solutions with  $\leq 5$  per cent difference in variance reduction from the best solution fall within depth ranges of  $\pm 1$  km from the best source depth (Fig. S2).

The November 2007 dike propagated southward in two phases. First, it propagated for  $\sim 18$  hrs along  $\sim 18$  km of the rift length followed by a 10 h stall in propagation. The second segment of the dike continued to propagate southward for  $\sim 15$  h along  $\sim 7$  km length of the rift (Belachew *et al.* 2011) (Fig. 4a). The propagation phase earthquakes for the November 2007 dike are predominantly of normal faulting type with varying amounts of non-double couple components (Fig. 4a, Table 4). Mechanisms 9 and 10, which are dominantly strike-slip type and with centroid depths of 6 km, are for earthquakes from the portion of the rift intruded by the second,

deeper segment of the November 2007 dike (Belachew *et al.* 2011). Event 9 occurred during propagation while event 10 occurred after the dike propagation stopped.

The October 2008 dike propagated northward for  $\sim 8$  h and intruded  $\sim 15$  km of the rift above the zone of maximum opening (8 m) in the 2005 mega-dike (Fig. 4b). For earthquakes related to the October 2008 dike intrusion 13 source mechanisms are determined (Fig. 4b, Table 4). Normal faulting mechanisms with smaller non-double couple components and less strike-slip sense of motion than the November 2007 dike are obtained. The October 2008 dike intruded the rift portion that has experienced up to 8 m opening during the September 2005 dike event. Thus, the area is more intensely fractured than the southern section where the November 2007 dike intruded.

The space-time distribution of the solutions with respect to the epicentral migration patterns shows all but three of the mechanisms are for the earthquakes that occurred during the propagation phase of the two dikes (Fig. 4). The 3 exceptions (events 10, 21 and 22) occurred after the dike propagation stopped. For both dikes, 17 of the 22 mechanisms are for earthquakes that have been classified as low-frequency earthquakes (Fig. S1). These low-frequency events are interpreted to have been caused by the interaction between faults and the dikes and/or associated fluids (Belachew *et al.* 2011).

Rupture length and width related to each event are estimated using the empirical relationships for  $M_w$  versus rupture length and width determined from inspection of regression curves for a global suite of normal fault data from continental rifts (Wells & Coppersmith 1994). Important to note is that most or all of the earthquakes in the catalog used to determine this empirical relation are tectonic earthquakes with no magmatic association. Incrementally accrued slip, increased fault length due to lateral propagation of dikes and the type of earthquakes considered are among several factors that result in discrepancies from slip estimates determined using the empirical relationships (Smith *et al.* 1996; Rowland *et al.* 2007). Therefore,

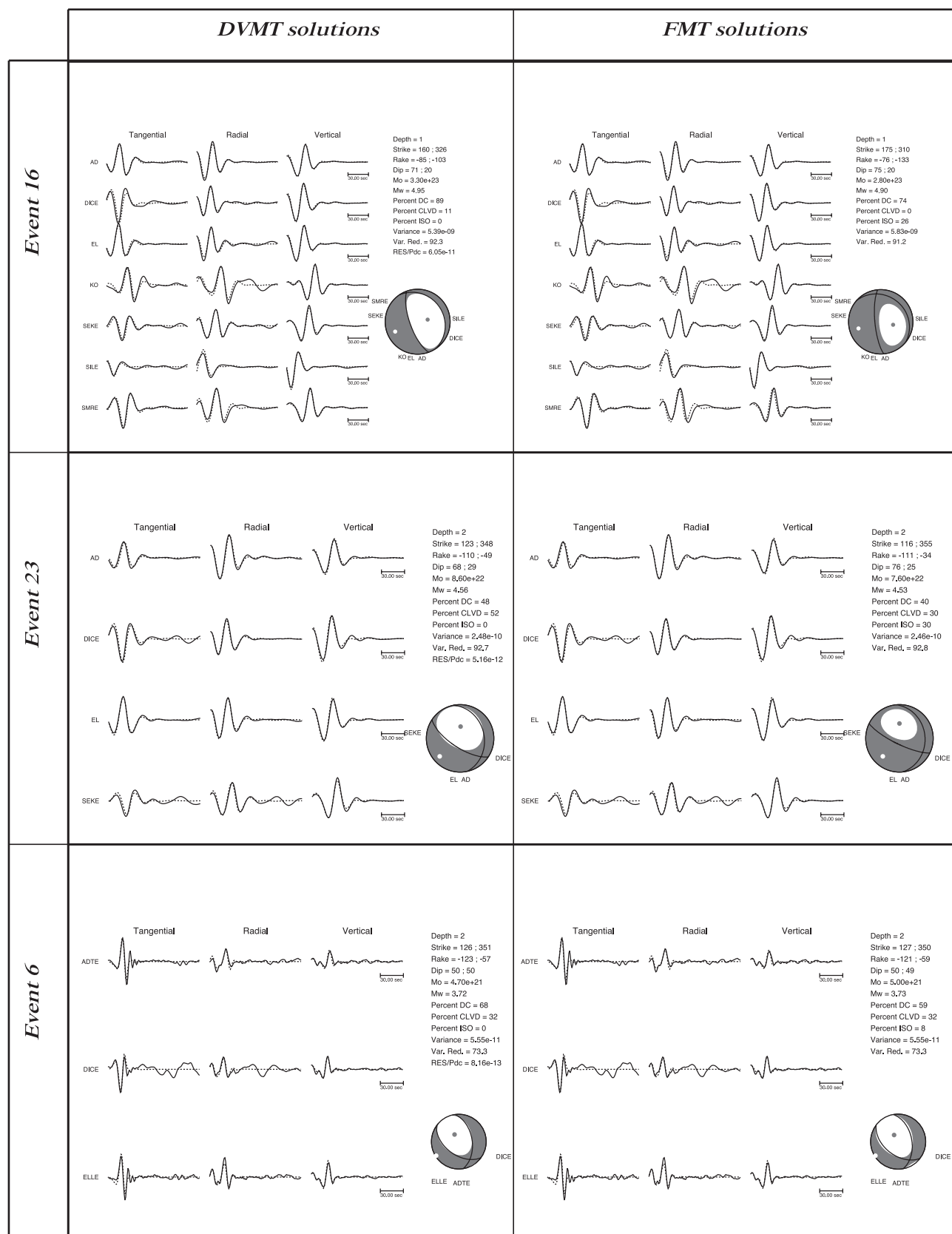


**Figure 2.** Sample waveform fits and associated DVMT and FMT solutions for events 6, 16 and 23, which illustrate the fits obtained for the different number of stations used. Data and synthetic waveforms are shown by solid and dashed lines, respectively. The strike, rake, and dip of the two nodal planes of the best double couple, the scalar seismic moment ( $M_0$ ), moment magnitude ( $M_w$ ), the percent double couple (DC), percent compensated linear vector dipole (CLVD), percent isotropic (ISO), the variance of the data to the model are provided. The beach balls are lower hemisphere projection.

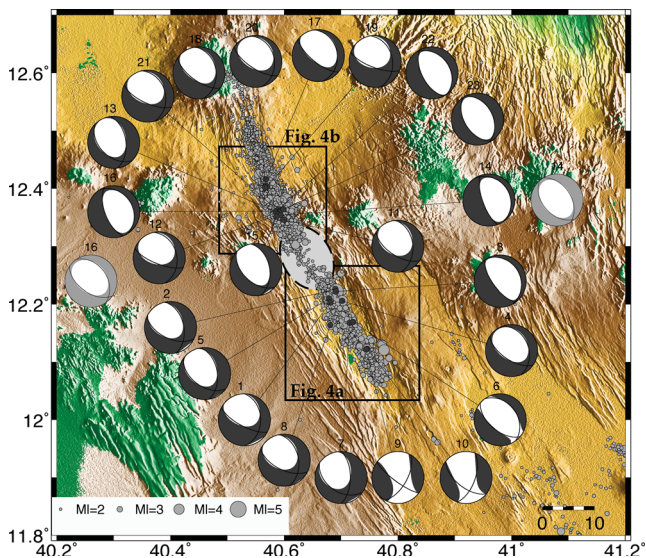


**Figure 3.** Plot of the locations and deviatoric source mechanisms determined for the 23 earthquakes in this study. Fault plane solutions are lower hemisphere projections. The best double-couple mechanisms are overlain on each beachball. The grey dots represent the earthquakes recorded between March 2007 and October 2009, and the locations of the earthquakes for which source mechanisms are determined are represented by darker dots. The shaded elliptical region around 12.3°N, 40.6°E is the surface projection of the location of the feeder zone for the multiple dikes that intruded the DMH rift segment as estimated by Belachew *et al.* (2011). The rectangles show the locations of Figs 4a and b. The numbers for the mechanisms are according to Table 2. Global CMT solutions for events 16 and 19 are shown in light grey fill. Earthquakes are scaled by magnitude.

our slip estimates using this relationship are minimum estimates that await statistical analyses of fault length-displacement analyses of Lidar data (J. Rowland, pers. comm. 2012). Normal faulting mechanisms are used in the calculation except for events 9 and 10 that are predominantly strike-slip type. These parameters and the scalar seismic moments are used to estimate the average fault slip through the equation for static seismic moment,  $M_0 = \mu SLW$  (Aki 1966), where  $S$  is the average fault slip,  $L$  is fault segment length,  $W$  is fault width and  $\mu$  is the rigidity elastic constant of the source region, which is usually taken as  $3 \times 10^{10}$  Pascal for crustal faults (Hanks & Kanamori 1979). The deviatoric scalar moment estimates are used since the moment values from the FMT inversions are higher due to the trade-offs between the elements of the moment tensor (e.g. Dreger & Woods 2002). The estimated fault parameters are given in Table 5.

Total slips of 0.8 m and 1.3 m are obtained for the array of faults that slipped during the November 2007 and October 2008 dikes, respectively. The earthquakes studied in this paper represent ~55 per cent of the total seismic moment release for both dikes, and all but four have source depths of <3 km from the source inversions (Table 3). Thus, surface faulting above the dikes accounts for most of the seismic energy release during dike intrusions. Estimates of slip derived from this subset of the largest earthquakes place a minimum bound on the total along-strike slip during the November 2007 and October 2008 dike intrusions. Normal fault slips summed along the length of the dike intrusion zone estimated from models of surface deformation are 1.9 m and 1.3 m for the 2007 and 2008 dike intrusions, respectively (Hamling *et al.* 2009). Comparison of the slips estimated from geodetic models and from seismic models suggests that most of the deformation above the dike occurs seismi-

cally through earthquakes with unusually low-frequency content, and it increases the seismic-geodetic deficit in terms of the dike inflation accommodating the rift opening.

## 5 DISCUSSION

Source mechanisms of some volcano-tectonic earthquakes are known to be complex, reflecting the possible superposition of volumetric changes caused by fluids, curved fault surfaces, and complex shear faulting (e.g. Julian *et al.* 1998; Dreger *et al.* 2000; McNutt 2005; Minson *et al.* 2007; Shuler & Ekström 2009). Likewise, multiple processes that may cause seismicity are associated with dike injection: migrating microseismicity at the crack tip during dike propagation; microseismicity in the wall rock adjacent to the dike caused by fluid pressures within the expanding dike; faulting above the dike that may or may not reach the surface. We analyzed waveforms of earthquakes occurring during and immediately after dike migration episodes along the incipient plate rupture zone in Afar. Consistent patterns in the source mechanisms reveal the basic characteristics of brittle failure and its distribution during dike intrusions along the length of the DMH rift segment, enabling us to distinguish earthquakes associated with faulting above the dike.

Several lines of evidence indicate that the largest ( $M_L \geq 3.5$ ) earthquakes during dike intrusions correspond to fault slips above the dikes. In all but 4 earthquakes from the segmented November 2007 dike, the best-fitting solution is located at depths of <3 km (Table 2). Two of the deeper earthquakes (events 9, 10) are predominantly strike-slip. Elastic dislocation models of surface displacements indicate that the November 2007 and October 2008 dikes reached to ~2 km subsurface (Grandin *et al.* 2009; Hamling *et al.* 2009), indicating that the ruptures initiate in the brittle rock layer above the dike. Given the low-frequency character of many of the earthquakes, and the rupture in a hot, degassing dike zone, we have inverted waveforms for non-double components. The non-double components may provide insight into the interaction of the fault with the top of the dike. Although the percentage CLVD and ISO components may vary, none of the best-fitting mechanisms indicate shear displacement in the wall rocks to the dike itself and at the propagating dike tip, as outlined below. Theory and observations show that dike intrusion places the wall rocks in compression, with microfracturing the main mode of stress release (Toda *et al.* 2002; Roman *et al.* 2004). Yet, none of the mechanisms determined have strike-slip and/or reverse faulting mechanisms with P-axes rotated ~90° from the regional maximum compressive stress direction typical of slip in the region surrounding the dike (e.g. Bonafede & Danesi 1997; Roman & Cashman 2006). Instead, the two strike-slip mechanisms (events 9 and 10) show rift perpendicular opening (Figs 3 and 4), and may indicate brittle failure around an asperity where the November 2007 stalled for ~10 hours. Although seismometers were located too far from the dikes to measure time variations in seismic anisotropy during dike intrusion, Keir *et al.* (2011) found a temporally stable and strong rift parallel anisotropy indicative of melt-filled cracks throughout the dike-inter dike periods. Dike tip earthquakes are expected to have strike-slip or normal faulting mechanisms, depending on the orientations of the principal stress axes (Ukawa & Tsukahara 1996), but the magnitudes of these migrating earthquake swarms are usually  $M_L < 2$  (e.g. Brandsdóttir & Einarsson 1979; Rubin 1995; Rubin & Gillard 1998). The time-distance relations of seismic moment release shows that the largest, commonly low-frequency earthquakes, occur minutes to hours after the passage of nearly continuous swarms of

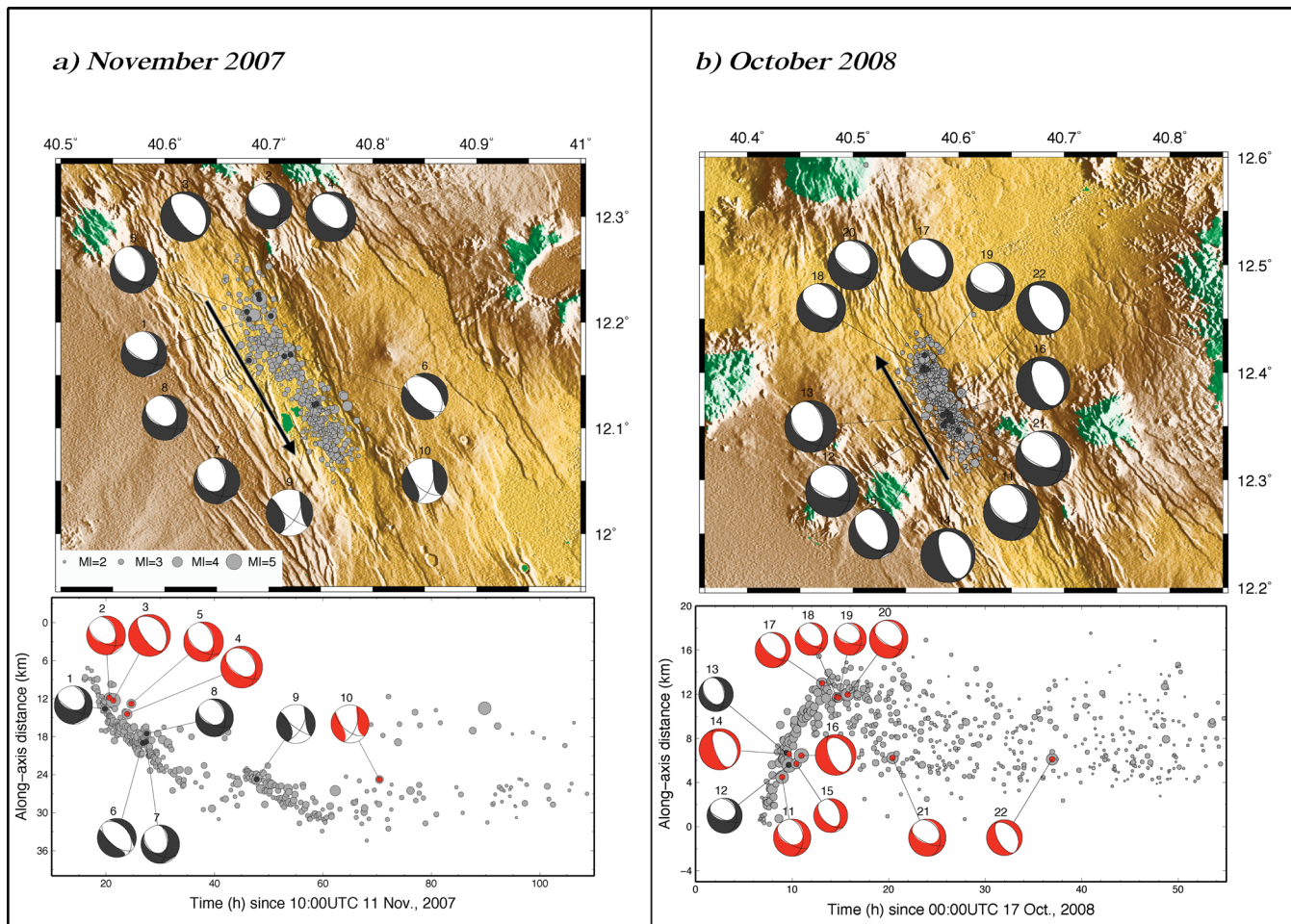


**Figure 4.** (a) (Top) Plot of epicenters and source mechanisms for earthquakes generated during the November 2007 dike intrusion. The numbering of the mechanism is according to Table 2 and similar to Fig. 3. Arrow shows the propagation direction of the dike inferred from seismicity migration. Earthquakes are scaled by magnitude, and the legend applies to all panels. (Bottom) Space-time distribution of the source mechanisms in relation to the along-axis southward migration of epicenters (modified from Belachew *et al.* 2011). The mechanisms with red compression zone represent the low-frequency earthquakes that have peak frequencies of  $\leq 2$  Hz. The seismicity distribution shows this dike is segmented with  $\sim 10$  h time gap between cessation of the first segment, and propagation of the 2nd deeper segment. (b) Same as in (a) but for October 2008 dike which propagated northwards.

microearthquakes ( $M_L < 2$ ) interpreted as the dike tip events (Belachew *et al.* 2011).

The shallow source depths of all but 4 of the earthquakes, the predominance of normal faulting mechanisms, and their temporal occurrence after the passage of the dike tip indicate that the largest earthquakes are associated with failure in the  $< 3$  km-thick brittle layer above the inflating dike. Given the significant non-double couple component of these earthquakes, their unusually low frequencies ( $\leq 2$  Hz) may indicate fluid interactions during fault rupture. The narrow spectral peaks exhibited by these LF earthquakes could also be caused by the resonance of fluid-filled cracks or conduits induced by pressure transients in the fluid (Aki *et al.* 1977; Chouet 1996, 2003; Kumagai & Chouet 1999), or slow-slip events with long source-time functions or may reflect brittle failure along a zone intersecting a fluid-filled crack (Lahr *et al.* 1994; Kawakatsu & Yamamoto 2007). Therefore, although not conclusive, the shallow source depths of most of the largest earthquakes, low-frequency content, observed surface fault displacements and the predominant normal faulting mechanisms all point to rupture initiation in the brittle rock layer above dikes. These observations indicate that normal faulting above the dike is by far the most energetic of the three dike intrusion processes.

A comparison of seismic and geodetic slip estimates due to normal faulting above dikes, and total seismic and geodetic moment release provide important clues to the plate boundary deformation and the formation of topography in this incipient seafloor spreading zone. The earthquakes are distributed along the length of the dike-intruded zone, and across a  $\sim 5$  km-wide zone. Field data and Lidar analyses indicate that surface faults that slipped during dike intrusions between September 2005 and March 2008 have a mean length of 2 km, and mean slip of 2 m (Rowland *et al.* 2007; J. Rowland, pers. comm. 2011). Thus, the rupture length estimates suggest that slip was accrued along multiple faults. But we cannot associate specific earthquakes with specific fault ruptures, given the dense faulting. The combined slip of the analyzed earthquakes is 1.3 m for the 15 km-long, northward propagating October 2008 dike, which is 1/3 more than that of 0.8 m for the 25 km-long, southward propagating November 2007 dike, crudely consistent with the smaller volume of the November 2007 dike as estimated from geodetic data (Hamling *et al.* 2009). Models of surface deformation indicate total normal fault slips of 1.9 m and 1.3 m for the November and October dikes, respectively. The geodetic and seismic slip estimates are identical for the October 2008 dike, whereas the total seismic slip estimate for the November 2007 dike is  $\sim 1/2$  that of the geodetic slip



**Table 5.** Estimates of rupture length, width, and slip for the 23 earthquakes.

Event	Mo ( $\times 10^{13}$ Nm)	Length (km)	Width (km)	Area (km <sup>2</sup> )	Slip (m)
1	26	0.36	0.66	0.2376	0.04
2	60	0.34	0.63	0.2142	0.09
3	1100	1.48	1.84	2.7232	0.13
4	110	0.51	0.85	0.4335	0.08
5	47	0.38	0.69	0.2622	0.06
6	36	0.34	0.63	0.2142	0.06
7	32	0.34	0.63	0.2142	0.05
8	24	0.27	0.75	0.2025	0.04
9	34	0.27	0.75	0.2025	0.06
10	23	0.24	0.49	0.1176	0.07
11	550	1.11	1.5	1.665	0.11
12	180	0.68	1.04	0.7072	0.08
13	150	0.65	1.01	0.6565	0.08
14	3300	2.31	2.56	5.9136	0.19
15	110	0.53	0.87	0.4611	0.08
16	2400	2.14	2.42	5.1788	0.15
10	210	0.73	1.1	0.803	0.09
18	62	0.5	0.83	0.415	0.05
19	30	0.44	0.76	0.3344	0.03
20	760	1.27	1.65	2.0955	0.12
21	380	1.02	1.4	1.428	0.09
22	450	0.74	1.12	0.8288	0.18
23	350	0.69	1.06	0.7314	0.16

estimate. The November 2007 dike intruded as two discrete dikes with the second segment being deeper and accounting for only 40 per cent of the total seismic energy release (Belachew *et al.* 2011). The difference in the slip estimates for the November dike could be due to modeling of the dike as one dike with no along-length variation in depth, leading to over-estimates of surface faulting for the second dike segment. For both dikes, the total seismic moment is almost entirely attributed to the very shallow normal fault mechanisms interpreted as surface faulting above the dike with minor contributions from faulting in the dike walls and tip. The total seismic moment is only  $\sim 3$  per cent of the total geodetic moment estimates, but consistent with the surface faulting component, indicating that dike inflation occurs largely aseismically. Our estimates are considered minimum estimates of total fault slip, based on comparisons of field observations of length and displacement of faults that slipped in the 2005–2008 dike intrusion events. Rowland *et al.* (2007) documented average slip of 2 m along subvertical faults that slipped during the 2005 dike intrusion, and used imagery to map surface faulting across a  $\sim 3$ –5 km zone. The maximum observed fault displacements of  $\sim 5$  m may have accrued through either incremental slip or increased fault length due to dike propagation (Rowland *et al.* 2007). Using the mean fault slip of 2 m and the Wells & Copper-smith (1994) scaling, Rowland *et al.* (2007) pointed out that an  $M_w$  6.5 earthquake would be predicted. Therefore, we consider our slip estimates using this relationship as minimum estimates that provoke a detailed comparison of fault length-displacement and earthquake scaling relations for faults that form above dikes.

## 6 CONCLUSIONS

We use several approaches to study source mechanisms for the largest magnitude earthquakes that occurred during two large volume dike intrusions in an incipient seafloor spreading centre in Afar. Most of these earthquakes for which the mechanisms are computed occurred during the propagation phase of the dikes, but after the

microearthquakes marking the passage of the dike tip. The best solutions show that most of the earthquakes do not have pure double couple mechanisms, and the CLVD components are significant with a possibility of some isotropic components. The best double couple mechanisms indicate rupture of faults parallel to the strike of surface faults in the DMH rift. Comparison of the detailed space-time relationship of the source mechanisms with the seismicity migration patterns and evaluation of existing models indicate that the largest earthquakes are generated most likely by faulting above dikes during the dike inflation stage, after the passage of the crack tip. The low-frequency nature and shallow depths of the earthquakes, and the significant non-double couple source components, suggest the possible involvement of aqueous and/or magmatic fluids in their generation. The smaller magnitude dike-induced earthquakes for which source mechanisms could not be determined in this study may be caused by shear failure ahead of the propagating dikes and/or microfracturing in the wall rocks. Our results indicate that faulting above the dikes during the propagation phase accounts for the majority of seismic energy release, and that plate boundary deformation by dike intrusion occurs aseismically. The seismicity patterns and source mechanisms during dike intrusions within the Afar rift zone demonstrate the role of dike intrusions in the creation and maintenance of rift valley topography.

## ACKNOWLEDGMENTS

We thank the Institute for Geophysics, Space Sciences and Astronomy, the Ethiopian Federal Government and the Afar Regional State for invaluable assistance throughout all stages of this project. Moment tensors were computed using the *tdmt-inv* package developed by Douglas Dreger of the Berkeley Seismological Laboratory, and Green's functions were computed using *FKRPROG* software developed by Chandan Saikia with URS Granger, Woodward Clyde Federal Services. We would like to thank Douglas Dreger for providing both the *tdmt-inv* package and the grid search codes, and Sarah Minson and Sierra Boyd for invaluable advice. Comments by Eiichi Fukuyama (Editor) and two anonymous reviewers helped us improve the manuscript. The support of National Science Foundation grant EAR-0635789; NERC grants NE/D008611/1, NE/D01039X/1, and NE/E007414/1 are gratefully acknowledged. Most of the figures are generated using *GMT* software (Wessel & Smith 1998). The seismic instruments were provided by the Incorporated Research Institutions for Seismology (IRIS) through the *PASSCAL* Instrument Centre at New Mexico Tech.

## REFERENCES

- Aki, K., 1966. Generation and propagation of G waves from the Niigata earthquake of June 16, 1964. Part II. Estimation of earthquake movement, release energy, and stress-strain drop from G wave spectrum, *Bull. Earthq. Res. Inst.*, **44**, 23–88.
- Aki, K., Fehler, M. & Des, S., 1977. Source mechanism of volcanic tremor: Fluid-driven crack models and their application to the 1963 Kilauea eruption, *J. Volcanol. Geotherm. Res.*, **2**, 259–287.
- Ayele, A. *et al.*, 2009. September 2005 mega-dike emplacement in the Manda-Harraro nascent oceanic rift (Afar depression), *Geophys. Res. Lett.*, **36**(L20306), doi:10.1029/2009GL039605.
- Barberi, F. & Varet, J., 1977. Volcanism of Afar: small-scale plate tectonics implication, *Geol. Soc. Am. Bull.*, **88**, 1251–1266.
- Belachew, M., Ebinger, C., Coté, D., Keir, D., Rowland, J.V., Hammond, J.O.S. & Ayele, A., 2011. Comparison of dike intrusions in an incipient seafloor-spreading segment in Afar, Ethiopia: Seismicity perspectives, *J. geophys. Res.*, **116**(B06405), doi:10.1029/2010JB007908.

- Bonafede, M. & Danesi, S., 1997. Near-field modifications of stress induced by dyke injection at shallow depth, *Geophys. J. Int.*, **130**, 435–448.
- Brandsdóttir, B. & Einarsson, P., 1979. Seismic activity associated with the September 1977 deflation of Krafla volcano in North-Eastern Iceland, *J. Volc. Geotherm. Res.*, **6**, 197–212.
- Chouet, B.A., 1996. Long-period volcano seismicity: its source and use in eruption forecasting, *Nature*, **380**, 309–316.
- Chouet, B.A., 2003. Volcano Seismology, *Pure appl. Geophys.*, **160**, 739–788.
- Dreger, D.S., Kraljic, H. & Johnston, M., 2000. Dilational processes accompanying earthquakes in the Long Valley Caldera, *Science*, **288**, 122–125.
- Dreger, D. & Woods, B., 2002. Regional distance seismic moment tensors of nuclear explosions, *Tectonophysics*, **356**, 139–156.
- Dreger, D. & Woods, B., 2002. Regional distance seismic moment tensors of nuclear explosions, *Tectonophysics*, **356**, 139–156.
- Ebinger, C.J. *et al.*, 2008. Capturing magma intrusion and faulting processes during continental rupture: Seismicity of the Dabbahu (Afar) rift, *Geophys. J. Int.*, **174**, 1138–1152.
- Ebinger, C.J., Ayele, A., Keir, D., Rowland, J., Yirgu, G., Wright, T., Belachew, M. & Hamling, I., 2010. Length and time scales of rift faulting and magma intrusion: The Afar rifting cycle from 2005 to present, *Annu. Rev. Earth Planet. Sci.*, **38**, 437–464.
- Grandin, R. *et al.*, 2009. September 2005 Manda Hararo-Dabbahu rifting event, Afar (Ethiopia): Constraints provided by geodetic data, *J. geophys. Res.*, **114**, doi:10.1029/2008JB005843.
- Grandin, R., Socquet, A., Jacques, E., Mazzoni, N., Chabaliere, J.B. & King, G.C.P., 2010. Sequence of rifting in Afar (Manda-Hararo rift, Ethiopia, 2005–2009): Timespace evolution and interactions between dikes from InSAR and static stress change modeling, *J. geophys. Res.*, **115**(B10413), doi:10.1029/2009JB000815.
- Grandin, R. *et al.*, 2011. Seismicity during lateral dike propagation: Insights from new data in the recent Manda Hararo–Dabbahu rifting episode (Afar, Ethiopia), *Geochem. Geophys. Geosyst.*, **12**(Q0AB08), doi:10.1029/2010GC003434.
- Hamling, I.J. *et al.*, 2009. Geodetic observations of the ongoing Dabbahu rifting episode: New dyke intrusions in 2006 and 2007, *Geophys. J. Int.*, **178**, 989–1003.
- Hamling, I.J., Wright, T.J., Calais, E., Bennati, L. & Lewi, E., 2010. Stress transfer between thirteen successive dyke intrusions in Ethiopia, *Nature Geoscience*, **3**, 713–717.
- Hanks, T.C. & Kanamori, H., 1979. A moment-magnitude scale, *J. geophys. Res.*, **84**, 2348–2350.
- Hayward, N.J. & Ebinger, C.J., 1996. Variations in the along-axis segmentation of the Afar Rift System, *Tectonics*, **15**, 244–257.
- Jacques, E., Ruegg, J.-C., L'epine, J.-C., Tapponnier, P., King, G.C.P. & Omar, A., 1999. Relocation of  $M > 3$  events of the 1989 Dobi sequence in Afar: evidence for earthquake migration, *Geophys. J. Int.*, **138**, 447–69.
- Jost, M.L. & Herrmann, R.B., 1989. A student's guide to and review of moment tensors, *Seismol. Res. Lett.*, **60**, 37–57.
- Julian, B.R. & Sipkin, S.A., 1985. Earthquake processes in the Long Valley Caldera area, California, *J. geophys. Res.*, **90**(13B), 11 155–11 169.
- Julian, B.R., Miller, A.D. & Foulger, G.R., 1998. Nondouble-couple earthquakes: 1. Theory, *Rev. Geophys.*, **36**, 525–549.
- Kawakatsu, H. & Yamamoto, M., 2007. Volcano seismology, in *Treatise on Geophysics. Earthquake Seismology*, pp. 389–420, Vol. 4, ed. Kamanori, H., Elsevier.
- Keir, D. *et al.*, 2009. Evidence for focused magmatic accretion at segment centers from lateral dike injections captured beneath the Red Sea rift in Afar, *Geology*, **37**, 59–62.
- Keir, D., Belachew, M., Ebinger, C.J., Kendall, J., Hammond, J.O.S., Stuart, G.W. & Ayele, A., 2011. Mapping the evolving strain field in the Afar Triple Junction using crustal anisotropy, *Nat. Commun.*, **2**(285), doi:10.1038/ncomms1287.
- Knopoff, L. & Randall, M.J., 1970. The compensated linear-vector: a possible mechanism for deep earthquakes, *J. geophys. Res.*, **75**, 4957–4963.
- Kumagai, H. & Chouet, B.A., 1999. The complex frequencies of long-period seismic events as probes of fluid composition beneath volcanos, *Geophys. J. Int.*, **138**, F7–F12.
- Lahr, J.C., Chouet, B.A., Stephens, C.D., Power, J.A. & Page, R.A., 1994. Earthquake classification, location, and error analysis in a volcanic environment: Implications for the magmatic system of the 1989–1990 eruptions at Redoubt Volcano, Alaska, *J. Volc. Geotherm. Res.*, **62**, 137–151.
- Manighetti, I., Tapponnier, P., Courtillot, V., Gallet, Y., Jacques, E. & Gillot, Y., 2001. Strain transfer between disconnected, propagating rifts in Afar, *J. geophys. Res.*, **106**, 13 613–13 665.
- McKenzie, D.P., Davis, D. & Molnar, P., 1970. Plate tectonics of the Red Sea and East Africa, *Nature*, **226**, 243–248.
- McNutt, S.R., 2005. Volcano Seismology, *Annu. Rev. Earth Planet. Sci.*, **33**, 461–491.
- Minson, S.E., Dreger, D.S., Bürgmann, R., Kanamori, H. & Larson, K.M., 2007. Seismically and geodetically determined nondouble-couple source mechanisms from the 2000 Miyakejima volcanic earthquake swarm, *J. geophys. Res.*, **112**, 10308, doi:10.1029/2006JB004847.
- Minson, S.E. & Dreger, D.S., 2008. Stable inversions for complete moment tensors, *Geophys. J. Int.*, **174**(2), 585–592.
- Nakano *et al.*, 2008. Waveform inversion in the frequency domain for the simultaneous determination of earthquake source mechanism and moment function, *Geophys. J. Int.*, **173**, 1000–1011.
- Pollard, D.D., Delaney, P.T., Duffield, W.A., Endo, E.T. & Okamura, A.T., 1983. Surface deformation in volcanic rift zones, *Tectonophysics*, **94**, 541–584.
- Roman, D.C., Moran, S.C., Power, J.A. & Cashman, K.V., 2004. Temporal and spatial variation of local stress fields before and after the 1992 eruptions of Crater Peak Vent, Mount Spurr Volcano, Alaska, *Seism. Soc. Am. Bull.*, **94**, doi:10.1785/0120030259.
- Roman, D.C., 2005. Numerical models of volcano-tectonic earthquake triggering on non-ideally oriented faults, *Geophys. Res. Lett.*, **32**(L02304), doi:10.1029/2004GL021549.
- Roman, D.C. & Cashman, K.V., 2006. The origin of volcano-tectonic earthquake swarms, *Geology*, **34**, 457–460.
- Rowland, J.V., Baker, E., Ebinger, C.J., Keir, D., Kidane, T., Biggs, J., Hayward, N. & Wright, T.J., 2007. Fault growth at a nascent slow-spreading ridge: 2005 Dabbahu rifting episode, Afar, *Geophys. J. Int.*, **171**, 1226–1246.
- Rubin, A.M. & Pollard, D.D., 1988. Dike-induced faulting in rift zones of Iceland and Afar, *Geology*, **16**, 413–416.
- Rubin, A.M., 1992. Dike-induced faulting and graben subsidence in volcanic rift zones, *J. geophys. Res.*, **97**(B2), 1839–1858.
- Rubin, A.M., 1995. Propagation of magma-filled cracks, *Annu. Rev. Earth Planet. Sci.*, **23**, 287–336.
- Rubin, A.M. & Gillard, D., 1998. Dike-induced earthquakes: Theoretical considerations, *J. geophys. Res.*, **103**(B5), 10 017–10 030.
- Rubin, A., Gillard, D. & Got, J., 1998. A reinterpretation of seismicity associated with the January 1983 dike intrusion at Kilauea volcano, Hawaii, *J. geophys. Res.*, **103**, 10003–10015.
- Saikia, C.K., 1994. Modified frequency-wavenumber algorithm for regional seismograms using Filon's quadrature: Modelling Lg waves in eastern North America, *Geophys. J. Int.*, **118**(1), 142–158.
- Shuler, A. & Ekström, G., 2009. Anomalous earthquakes associated with Nyiragongo Volcano: Observations and potential mechanisms, *J. Volc. Geotherm. Res.*, **181**, 219–230.
- Smith, R.P., Jackson, S.M. & Hackett, W.R., 1996. Paleoseismology and seismic hazards evaluation in extensional volcanic terrains, *J. geophys. Res.*, **101**, 6277–6292, *Soc. Amer.*, **117**, 846–864.
- Templeton, D.C. & Dreger, D.S., 2006. Non-double-couple earthquakes in the Long Valley volcanic region, *Bull. seism. Soc. Am.*, **96**(1), 69–79.
- Toda, S., Stein, R.S. & Sagiya, T., 2002. Evidence from the AD 2000 Izu islands earthquake swarm that stressing rate governs seismicity, *Nature*, **419**, 58–61.
- Ukawa, M. & Tsukahara, H., 1996. Earthquake swarms and dike intrusions off the east coast of Izu Peninsula, central Japan, *Tectonophysics*, **253**, 285–303.

- Vigny, C., Huchon, P., Ruegg, J.-C., Khanbari, K. & Asfaw, L.M., 2006. Confirmation of Arabia plate slow motion by new GPS data in Yemen, *J. geophys. Res.*, **111**(B02402), doi:10.1029/2004JB003229.
- Wells, D.L. & Coppersmith, K.J., 1994. New empirical relationships among magnitude, rupture length, rupture width, rupture area, and surface displacement, *Bull. seism. Soc. Am.*, **84**, 974–1002.
- Wessel, P. & Smith, W.H.F., 1998. New, improved version of generic mapping tools released, *EOS, Trans. Am. geophys. Un.*, **79**, 579, doi:10.1029/98EO00426.
- Wills, S. & Buck, W.R., 1997. Stress-field rotation and rooted detachment faults: A Coulomb failure analysis, *J. geophys. Res.*, **102**, 20 503–20 514.
- Wright, T.J., Ebinger, C., Biggs, J., Ayele, A., Yirgu, G., Keir, D. & Stork, A., 2006. Magma maintained rift segmentation at continental rupture in the 2005 Afar dyking episode, *Nature*, **442**, 291–294.

## SUPPORTING INFORMATION

Additional Supporting Information may be found in the online version of this article:

**Figure S1.** Plot showing the difference between the spectral contents of example earthquakes classified as low-frequency earthquake (Event 1) with peak frequency of  $\sim 2$  Hz (top, a and b) and tectonic earthquake (Event 2) with peak frequency  $> 2$  Hz (bottom, c and d) both recorded at station FINE and located close to each other. Note the clear *P*-wave onset the low-frequency waveform. The station FINE is located at  $12.07^{\circ}\text{N}$  and  $40.32^{\circ}\text{E}$ . Event

#1 ( $12.24^{\circ}\text{N}$ ,  $40.66^{\circ}\text{E}$ ,  $M_L = 3$ ) and Event #2 ( $12.22^{\circ}\text{N}$ ,  $40.69^{\circ}\text{E}$ ,  $M_L = 4.6$ ).

**Figure S2.** Comparison of the DVMT solutions with depth showing the depth dependency. The red beach balls are the solutions with best goodness of fit to data (variance reduction). For all but 4 earthquakes the best depths are  $< 3$  km. Beachballs are scaled by magnitude and the variance reductions for each solution are also shown.

**Table S1.** Location of seismic stations used for the source mechanism study.

**Table S2.** DC solutions for the studied earthquakes (Scalar moment ( $M_0$ ) is given in  $10^{13}$  Nm). Note that for DC mechanisms  $M_{0\text{iso}} = 0$  by definition.

**Table S3.** DC + ISO solutions for the studied earthquakes (Scalar moments ( $M_0$ ) and isotropic moments ( $M_{0\text{iso}}$ ) are given in  $10^{13}$  Nm).

**Table S4.** DVMT solutions for the studied earthquakes (Scalar moment ( $M_0$ ) is given in  $10^{13}$  Nm). Note that for DVMT solutions  $M_{0\text{iso}} = 0$  by definition.

**Table S5.** FMT solutions for the studied earthquakes (Scalar moments ( $M_0$ ) and isotropic moments ( $M_{0\text{iso}}$ ) are given in  $10^{13}$  Nm). (<http://gji.oxfordjournals.org/lookup/suppl/doi:10.1093/gji/ggs076/-/DC1>)

Please note: Oxford University Press are not responsible for the content or functionality of any supporting materials supplied by the authors. Any queries (other than missing material) should be directed to the corresponding author for the article.